Nanoscience and Nanotechnology Letters
Vol. 3, 561–567, 2011

ESR Microscopy for Biological and Biomedical Applications

C. S. Shin[1,2,†], C. R. Dunnam[1,2], P. P. Borbat[1,2], B. Dzikovski[1,2], E. D. Barth[3], H. J. Halpern[3], and J. H. Freed[1,2,*]

[1] *National Biomedical Center for Advanced ESR Technology,* [2] *Department of Chemistry and Chemical Biology, Cornell University, Ithaca, NY 14853, USA*
[3] *Center for EPR Imaging In Vivo Physiology, Department of Radiation and Cellular Oncology, University of Chicago, Chicago, IL 60637, USA*

We report on electron-spin resonance microscopy (ESRM) providing sub-micron resolution (∼700 nm) with a high spin concentration sample, i.e., lithium phthalocyanine (LiPc) crystal. For biomedical applications of our ESRM, we have imaged samples containing rat basophilic leukemia (RBL) cells as well as cancerous tissue samples with a resolution of several microns using a water soluble spin probe, Trityl_OX063_d24. Phantom samples with the nitroxide spin label, ^{15}N PDT, were also imaged to demonstrate that nitroxides, which are commonly used as spin labels, may also be used for ESRM applications. ESRM tissue imaging would therefore be valuable for diagnostic or therapeutic purposes. Also, ESRM can be used to study the motility or the metabolism of cells in various environments. With further modification and/or improvement of imaging probe and spectrometer instrumentation sub-micron biological images should be obtainable, thereby providing a useful tool for various biomedical applications.

Keywords: ESRM, Sub-Micron Imaging, LiPc, Trityl, Nitroxides, Tissue Imaging, Cell Imaging, Prostate Cancer, Cell Motility, Cell Metabolism.

1. INTRODUCTION

Electron paramagnetic/spin resonance (EPR or ESR) spectroscopy and imaging have been extensively employed in many areas in physics, chemistry and biology. In order to enhance the detection sensitivity and the resolution of the ESR image a variety of detection methods, such as magnetic resonance force microscopy (MRFM), scanning tunneling microscopy ESR (STM-ESR), optically detected ESR (ODESR), or using semiconductor quantum dots, hall sensors, superconducting quantum interference devices (SQUID's), etc. have been explored with the hope of sensing or imaging individual molecules to extend the understanding of various chemical and/or biological systems. Recently, it has been reported that MRFM can probe a single electron spin[1] and image the proton density in an individual tobacco mosaic virus with better than 10 nm resolution;[2] also the possibility of observing commonly used electron spin probes by MRFM has been demonstrated.[3] But these MRFM studies required extreme conditions such as ultra-high vacuum and cryogenic temperatures, which may not be desirable for biological applications. ODESR, in contrast, is known to be capable of single spin detection under ambient conditions. Single spin imaging by ODESR has been demonstrated using nitrogen-vacancy (NV) defect color centers in diamond for magnetic resonance imaging applications with ∼20 nm resolution[4] and nano-scale magnetometry applications with ∼5 nm resolution under ambient conditions.[5] This is possible due to the high spin detection sensitivity of the optical detection technique and its long electron spin coherence time, e.g., $T_2 \sim 1.8$ ms, even at room temperature,[6] for the NV defect in ultrapure chemical vapor deposition (CVD) diamond with a low concentration of nuclear spin impurities, ∼0.3% of ^{13}C.

For biological and biomedical applications, conventional inductive detection methods via pickup coil or MW resonator are less sensitive than other non-conventional detection methods such as MRFM, SQUID or ODESR, but are still promising methodologies in microscopy applications for *in vivo* samples at ambient conditions and physiological temperatures.

*Author to whom correspondence should be addressed.
†Present address: Materials Sciences Division, Lawrence Berkeley National Laboratory, Berkeley, CA 94720, USA.

But the shorter T_2 of electron spins, compared to the T_2 of nuclear spins, has historically made ESR imaging under ambient conditions a challenging proposition. Despite the short T_2 of electron spin probes, recent advances in microwave (MW) technology and devices have allowed researchers to develop continuous wave (CW) ESR imaging (ESRI), as well as single point imaging (SPI) based on spin echoes or free induction decays for small animal imaging in the low ESR frequency regime (typically 0.25–1 GHz).[7–9] Furthermore, high resolution pulsed ESR microscopy (ESRM) has been developed by Blank, Freed and co-workers using a high Q dielectric resonator at higher frequencies of 9 and 16 GHz.[10–12] High resolution ESRM can detect $\sim 10^7$ spins with resolution of a few microns in about an hour, which is $\sim$5 orders of magnitude better than conventional NMR microscopy with micro coil detection.[10] This is mainly due to the much larger dipole moment of the electron spin, the high quality factor of the resonator and application of advanced MW technology and devices. ESR spectroscopy is also known to be very sensitive to molecular dynamics, leading to rich information about the sample.[13] The large electron gyromagnetic ratio allows one to use a low-cost electromagnet (0.3–0.6 T) for ESRM, rather than an expensive superconducting magnet as required for NMR microscopy.

Here we report first on our ESRM of sub-micron resolution with a high spin concentration sample, i.e., lithium phthalocyanine (LiPc) crystal, which has a spin density of $\sim 10^8$ spins per μm^3 and a relatively long T_2 of $2\sim4$ μs.[10, 14] To illustrate potential biological and biomedical applications, we imaged biological tissue samples, as well as cells, with a few microns resolution. In these cases, water soluble spin probes, such as trityl or nitroxide are favored with concentrations of $\sim$2 mM or less. This is due to the fact that higher spin concentrations induce spin-spin interactions that reduce the T_2 of the spin in the sample. In 1 mM of Trityl, there are about 6×10^5 spins per μm^3. Such a low density of spins in the liquid sample usually limits the resolution of our current ESRM to a few microns. Nonetheless, current studies indicate that resolution down to a micron with a liquid spin sample can be achieved in the near future by improving the sensitivity of the imaging probe and spectrometer, as noted below.

ESRM images with micron resolution could be used to study the architecture of various tissue samples. For example, information on tissue architecture is very important for cancer research, where one should be able to distinguish malignant tissue from benign tissue.[15] Details of the local environment including patterns of microviscosity, uniquely measurable with ESR, may shed other, new light on the nature of the malignant tissue milieu.[16] With modification of the current imaging probe of our ESRM, fresh tissue could also be studied for oxygen-radical imaging, which would give further information such as tissue metabolism.[17] Motility of biological cells in various environments, e.g., chemical gradients in blood vessels or in interstitial fluids can reveal various metastasis of diseases and the curing mechanism of damaged tissue structure.[18–20] ESR microscopy could be employed for such applications.

2. PULSED ESRM SYSTEM AT 15 GHz AND SUB-MICRON RESOLUTION OF ESRM IMAGING WITH HIGH CONCENTRATION SPIN SAMPLE

In EPRI or ESRM, as in MRI or NMR microscopy, the spin sample is subjected to a 3-dimensional magnetic field gradient, which encodes the spatial information in the resulting magnetic resonance spectrum, from which the magnetic resonance image is obtained. Electron spins are usually introduced into the sample, similar in principle to injecting dye molecules in fluorescence microscopy. For *in vivo* samples using trityls, spins were injected into mice intravenously (IV) via a tail vein.

Our pulsed ESRM spectrometer is composed of several major components, i.e., a home-built pulsed MW bridge, a home-built high current pulse gradient driver with high voltage pre-regulator, a timing card, a signal digitizer, imaging probes, and a high-homogeneity electromagnet with field-frequency lock.[10, 11, 21] In the imaging probe, a double stacked dielectric resonator was nested inside a 3-dimensional set of magnetic field gradient coils. The X gradient coil is a standard Maxwell pair, and the Y, Z gradient coils are of Golay design. Inductance values are $1\sim2$ μH for the X and Y coils, and ~5 μH for the Z coil. The pulse imaging sequence can be either a standard spin echo or an FID with appropriate phase cycling. Recent upgrades of the MW bridge and the optimization of the coupling efficiency of the MW resonator have improved the sensitivity of the spectrometer, which has allowed us to obtain submicron resolution of the ESRM image. With modification of pulse gradient driver and transmission lines of the gradient coil sets, current pulses with peak amplitudes of 55 A can be discharged into the gradient coils. A fast constant current switch upgrade has been employed for the Z gradient coils to provide the frequency-encoding gradient, which reduces the heat dissipation by a factor of $5\sim10$ depending on the pulse repetition rate. The imaging software program was developed as a user friendly LabVIEW virtual instrument, with Matlab being employed for the real-time and post data processing, and graphical presentation. Efficient memory usage of the imaging program permits an image size as large as $450 \times 450 \times 64$ voxels in the X, Y and Z directions, respectively. Real time data processing allows one to optimize the imaging parameters conveniently. Two processor controllers are employed in the ESRM system to monitor and maintain the temperatures of the resonator and gradient coil sets by controlling the flow rate of cold gas from a dry ice bath or refrigerant cold bath. With this temperature control, samples can be imaged over a temperature range

of −15 to 25 °C. Sample specimens are sealed in a flat or cylindrical holder that is inserted between the resonators for imaging. Further descriptions of the basic instrumentation systems can be found elsewhere,[10, 11, 22] therefore only key system upgrades will be described here.

Sub-micron resolution imaging requires that very large (pulsed) magnetic field gradients be applied to the spin samples. For this purpose, a relatively large capacitance of 51 nF is charged by a high voltage precharging circuit up to 425 V, and subsequently discharged into the gradient coils; the resulting current waveform is a half cycle of a sine wave with peak current of up to ∼55 A to the X gradient coils for ca 1 μs duration, and up to ∼38 A to the Y gradient coils for ca 1.4 μs duration. The estimated peak gradient fields are ∼75 T/m along the X axis and ∼47 T/m along the Y axis. In order to guarantee the linearity of the gradient field, a special program is used to provide pre-experiment calibration data for the X and Y gradient coils.

With a LiPc crystal of $\sim 55 \times 67 \times 15$ μm in the sample holder, an ESRM image was obtained with an estimated resolution of $\sim 0.7 \times 0.75 \times 7.5$ μm as shown in Figure 1. This is a factor of 3 improvement with respect to voxel size from a recent report featuring a different resonator design ($\sim 0.95 \times 1.1 \times 12.58$ μm),[23] and a factor of 20 improvement over our previous results with the current resonator design ($3 \times 3 \times 8$ μm).[22] We measured the spin concentration in the LiPc phantom sample by comparing the EPR absorption spectra of the LiPc sample with a 0.4 mM solution of ^{15}N perdeuterated tempone (PDT) (data not shown). The measured LiPc sample has $\sim 0.96 \times 10^8$ spins per μm^3, which is very close to the reported concentration, i.e., $\sim 1 \times 10^8$ spins per μm^3.[10] Various LiPc phantom samples were prepared for calibration and the demonstration of high resolution micro-imaging. The T_2 of deoxygenated LiPc was reported to be ∼2.5 μs at 250 MHz,[14] but depending on the LiPc crystals used, we have measured T_2 as large as 4.8 μs at 15 GHz after de-oxygenation in a glove box.

To avoid excessive coil heating and consequent detuning due to resonator temperature change, the pulse repetition rate was reduced to 500 Hz. After 50 averages with 8-step phase cycling, i.e., Bi-phase and CYCLOPS, the single voxel SNR was found to be ∼17. Image size is $250 \times 250 \times 64$ in the X, Y and Z axes, so the total experimental time (involving 50 averages of 8-step phase cycling per gradient set) due to the low repetition rate was ∼14 hr, but the effective data acquisition time is only ∼20 min, which would correspond to a 20 KHz repetition rate. This long experimental time is mainly due to the "dead time" necessary to dissipate excess heat from the gradient coil sets, which is consequently important in minimizing resonant frequency drift of the relatively high temperature coefficient dielectric resonator. For example, the resonance frequency can drift by ∼10 MHz per °C change at ∼15 GHz.[24] With a Q of ∼500 and a resonator

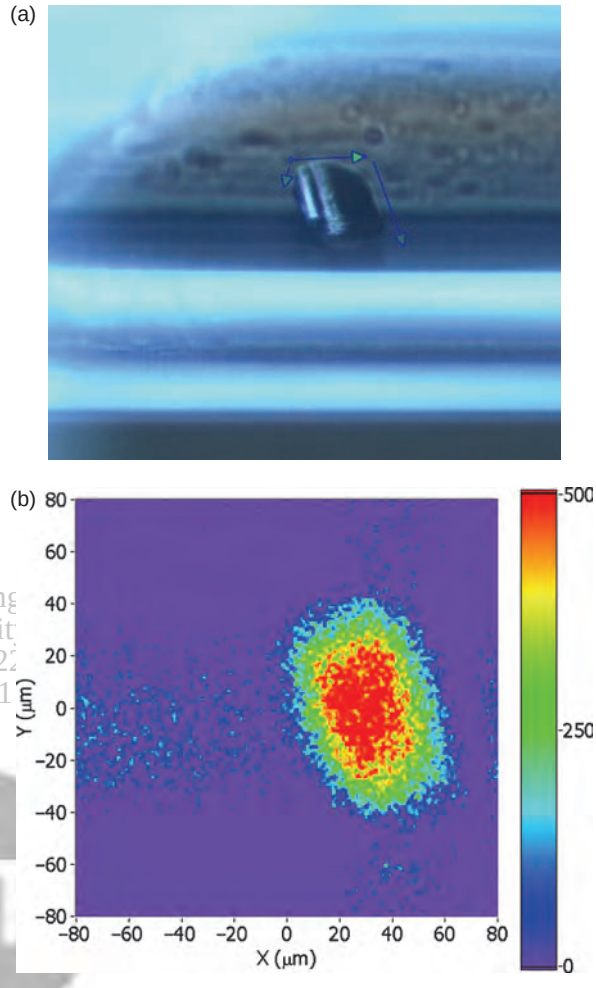

Fig. 1. (a) Optical image of LiPc crystal in glass capillary. LiPc crystal is $\sim 55 \times 67 \times 15$ μm. (b) Sub-micron ESRM image of LiPc sample. Measured spin concentration is $\sim 0.96 \times 10^8$ spins per μm^3, estimated voxel size (or resolution) is $\sim 0.7 \times 0.75 \times 7.5$ μm and estimated SNR (signal to RMS noise) after 50 signal averages is ∼17. Overall image size is $250 \times 250 \times 64$.

bandwidth of ∼30 MHz, the required temperature stability must be within ±1.5 °C. To illustrate the reduction in collection time that is possible, lower resolution images, e.g., $3 \times 3 \times 7$ μm were obtained without signal averaging, but using a 2-step phase cycle, as shown in Figure 2. Total experimental time was ∼30 seconds with a SNR of ∼12. In this case, heat dissipation of the coil sets was much less than for the sub-micron resolution image, because the pulse gradients required are not so intense, so the pulse repetition rate could be increased to 5 kHz. Therefore we conclude that, by improving the heat dissipation efficiency of the gradient coils by a factor of 10∼20, sub-micron-resolved images could be obtained in less than one hour.

Further performance enhancement will be obtained by modifying the existing haversine pulse gradient driver with improved electronic components, better heat sinking, etc. With an upgraded gradient driver, if detection sensitivity is not the primary limit of the system, close to optical

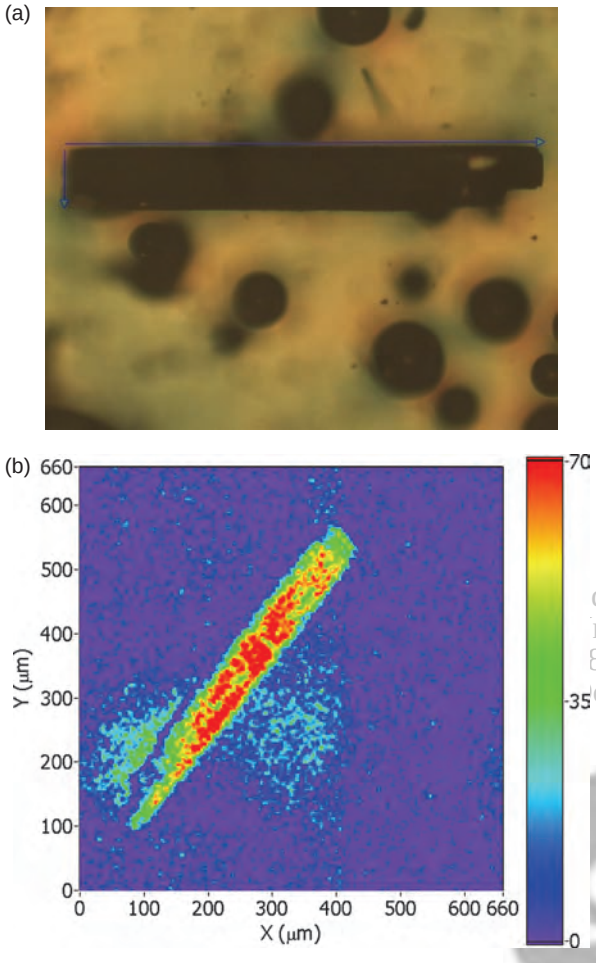

Fig. 2. (a) Optical image of LiPc crystal of $\sim 514 \times 63 \times 21$ μm in silicon sample holder (b) ESRM image of LiPc sample with estimated voxel resolution of $3 \times 3 \times 7$ μm, and overall image size is $220 \times 220 \times 128$. Image was obtained with 2-step phase cycling, but without any signal averaging. Total experimental time is ~30 seconds with pulse repetition rate of 5 kHz.

microscopy resolution, e.g., ~300 nm should be obtained. With such an improvement, more intense and shorter gradient pulses could be applied to the X, and Y gradient coils. This is an important upgrade path because the gradient pulses are supplied between the two MW pulses in an echo sequence or after the MW pulse in an FID sequence; with gradient pulses of higher peak intensity and shorter duration the recording of the signal could be initiated at a shorter time after the MW pulse. This would be beneficial for spin probes with short T_2, such as nitroxides ($T_2 <\sim 650$ ns), which are commonly used for spin labeling of biological systems in ESR spectroscopy. For spin probes with T_2^* close to T_2, ESRM based on FID's can give additional improvement in the signal amplitude, due to the shorter decay time of the FID by a factor of 2. In principle, FID-based imaging may provide further improvements by allowing recording of the signal immediately after the MW pulse and the receiver dead time, but this mode of acquisition requires well-shaped frequency gradients in all X, Y and Z axes. A suitable constant-amplitude gradient driver system recently designed for this purpose is presently under test. Finally, in FID-based imaging, higher B_o field stability is generally required; otherwise excessive image artifacts may be induced due to slight but unavoidable interference of the strong gradient field with the B_o field regulation system.

3. ESRM FOR BIOLOGICAL OR BIOMEDICAL APPLICATIONS

For biological and biomedical applications, water soluble spins probes such as Trityl are commonly used for CW EPRI and ESRM.[22, 25, 26] De-oxygenated ~1 mM Trityl in 5 mM NaOH has a narrow single absorption peak of ~120 mG at 9 GHz, corresponding to a relatively long T_2 of ~4 μs at 15 GHz. Using this Trityl spin probe, relevant parameters, such as viscosity, molecular self diffusion, or partial oxygen pressure can be imaged in various biological samples.

In order to demonstrate a biomedical application of ESRM, we imaged a cancerous mouse tissue sample. Our goal was to evaluate the microscopic heterogeneity of the spin concentrations in the cancerous tissue, which may induce spectral line-broadening or T_2 decrease due to spin-spin interactions. The tissue sample was prepared as follows: PC3 human prostate cancer was grown on the leg of an athymic nude mouse. Then, the mouse was injected IV with 0.5 mL of 70 mM Trityl OX063_d24 (FW 1451), and imaged with low frequency EPRI at the University of Chicago. After euthanasia, the leg was severed from the animal and subsequently frozen in liquid isopentane/nitrogen. Frozen tissue was then cryo-sectioned to provide a 60 μm thick tissue slice, 1.5 mm wide and ~2 mm in length. It was then loaded into the flat capillary sample holder of ID ~ 0.2×2 mm. The sample holder with frozen tissue was then sealed with UV epoxy in an anaerobic chamber with less than 1000 ppm oxygen concentration. The tissue sample was imaged at ACERT by ESRM as shown in Figure 3. The estimated resolution was $20 \times 20 \times 20$ microns.

A series of images were obtained with various interpulse τ values, e.g., 925 ns, 1025 ns, 1125 ns, etc., from which a spin concentration image and a T_2 image could be obtained to evaluate the heterogeneity of the Trityl concentration in the sample and the T_2 variation due to the concentration. Each pixel of these images for different τ's were fitted to an exponential decay curve to determine the amplitude and T_2 of the corresponding image pixel, leading to an amplitude image and a T_2 image, as shown in Figures 3(e) and (f), respectively. There is liquid that is evident in the optical image exterior to the tissue that is attributed to moisture condensed during the loading and sealing procedures conducted in a subzero °C environment. When the frozen sample was thawed, some of the Trityl

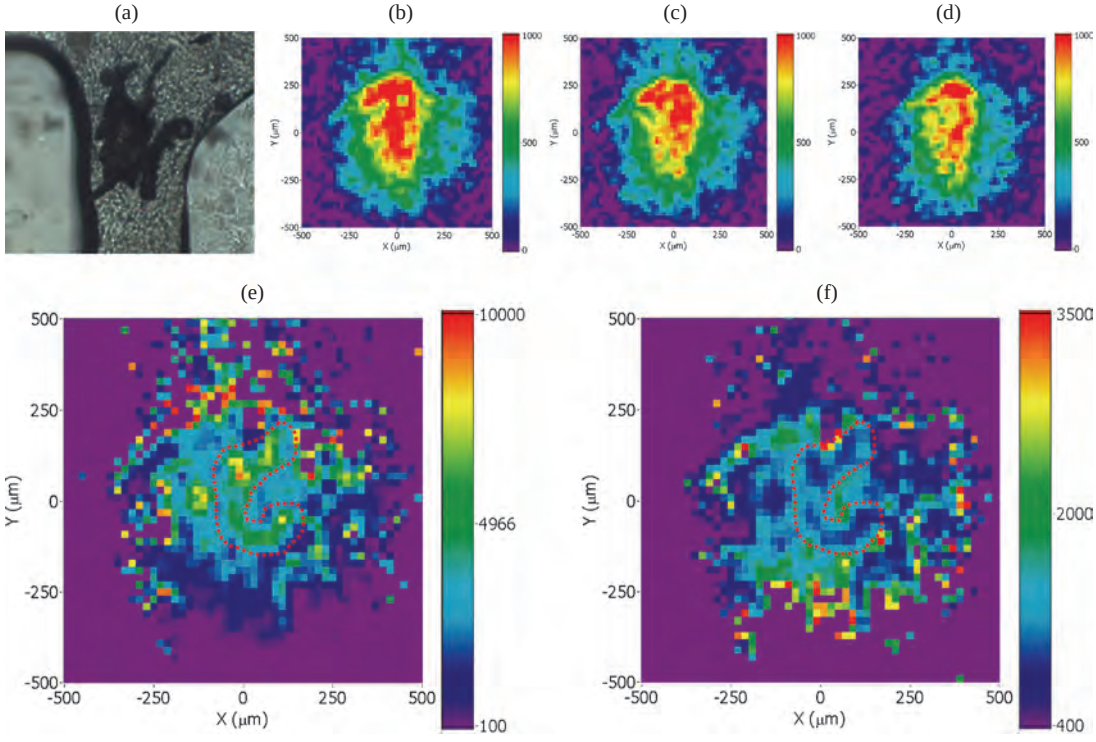

Fig. 3. (a) Optical image of mouse leg tissue with PC3 tumor. ESRM images with (b) $\tau = 925$ ns, (c) $\tau = 1025$ ns, (d) $\tau = 1125$ ns, (e) amplitude map (intensity bar corresponds to signal amplitude in arbitrary units) and (f) T_2 map (intensity bar corresponds to nanoseconds). Red dashed region in (e) and (f) corresponds to the region where spin concentration is higher, and T_2 is shorter than in other areas due to the spin-spin interactions. Estimated resolution is $20 \times 20 \times 20$ microns.

spins then began to diffuse from the tissue into the surrounding water, leading to ESR signals from the exterior of the tissue. All images were obtained at 20 °C. Trityl-loaded cancerous tissue, marked in the red dashed line in the amplitude image, shows higher spin concentration than the surrounding water solution by a factor of 2 or more, but the same marked area in the T_2 image also shows a shorter T_2 than the surrounding area. The average T_2 of the sample was ~1.4 μs. The shorter T_2 of ~900 ns in the marked area can be attributed to effects of spin-spin interaction due to the higher spin concentration, corresponding to higher extrapolated $\tau = 0$ amplitude. From these images, information such as partial oxygen pressure, viscosity and other parameters could be obtained for diagnostic or therapeutic purposes.

Since common Trityl spin probes are negatively charged, they are not permeable to the cell membrane.[27] Therefore, using these spin probes, e.g., Trityl OX063_d24, a negative ESRM image was obtained as shown in Figure 4. In this experiment, RBL cells were contained in ~1 mM Trityl OX063_d24 solutions in a pellet. A typical cell size is ~10 μm in diameter, and the estimated resolution of the ESRM image was $\sim 3 \times 3 \times 10$ μm, resulting in an image where cells are identified as negative dots surrounded by signal from the exterior Trityl solution. This negative imaging may be used to study the motility of the various cells in different environments, such as a chemical gradient in blood or interstitial fluids. Recently, an esterified Trityl was reported for intracellular oxygen level applications, which can be used to obtain positive ESRM images of the cell.[28] With improvements in the sensitivity of ESRM, these spin probes could be used to image the intracellular oxygen distribution of individual cells. This would provide useful information relating to cell metabolism, etc.

Due to their excellent compatibility with various biological systems, nitroxides have been used in ESR spectroscopy as spin labels in many biological samples, such as proteins, cells and vesicles. But hyperfine splittings and a relatively short T_2 make use of nitroxide spin labels difficult for imaging applications. However, Hyodo et al. recently reported ESR imaging of ^{15}N PDT spin labels in mouse studies, based on single point pulsed imaging.[29] We investigated various nitroxides for the possibility of ESRM applications. As shown in Figure 5, a phantom sample with ~0.5 mM ^{15}N PDT in deoxygenated water solution was prepared in a thin glass capillary with ID of ~210 μm, and was imaged by spin echoes. The measured T_2 was ~650 ns, and the estimated resolution is $\sim 10 \times 10 \times 50$ μm.

The T_2^* is comparable to T_2 for ^{15}N PDT, so that ESRM imaging based on FID's should improve the SNR as previously mentioned due to the factor of 2 difference in the exponent of the FID signal decay curve. Shorter and more

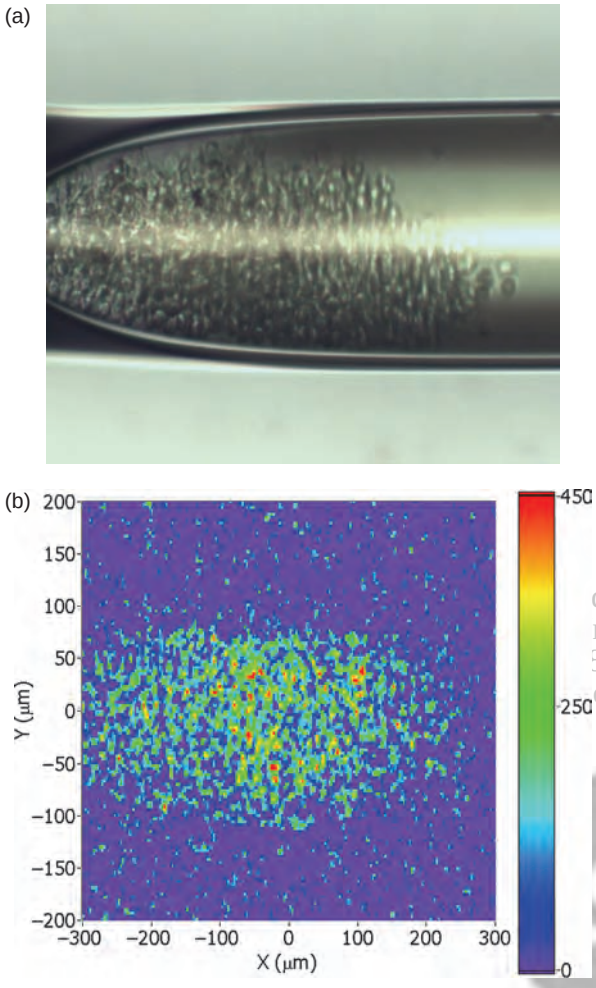

Fig. 4. (a) Optical image of a pellet containing RBL cells (∼10 μm in diameter) in the presence of ∼1 mM Trityl OX063_d24, (b) ESRM image of RBL cell sample. Estimated voxel size is $\sim 3 \times 3 \times 10$ μm. Cells are shown as dots of various sizes in the ESRM image.

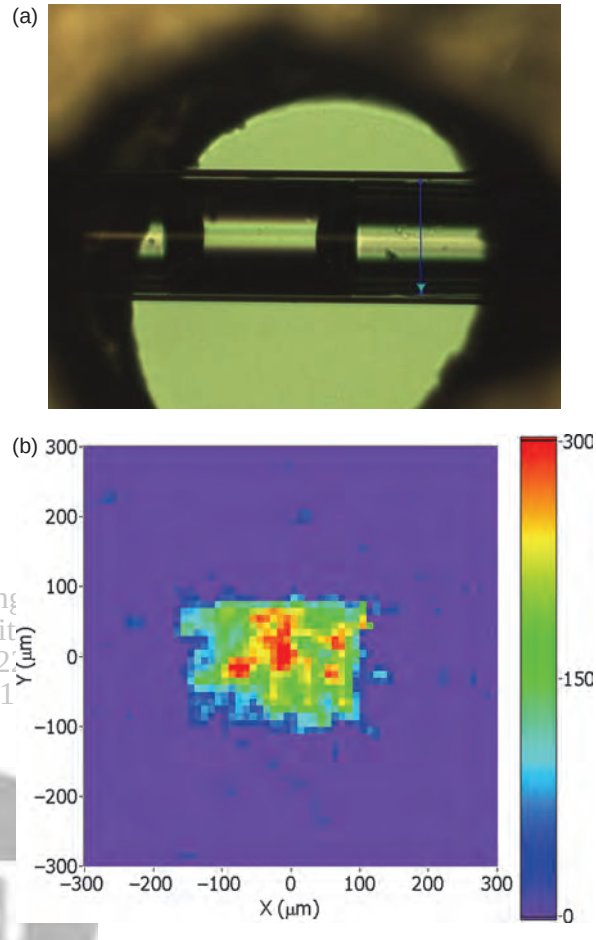

Fig. 5. (a) Optical image of ∼0.5 mM ^{15}N PDT in de-oxygenated water (arrow bar is 210 μm), (b) ESRM image after 5,000 signal averages at 14 kHz pulse repetition rate with 8-step phase cycling. Estimated resolution is $\sim 10 \times 10 \times 50$ μm with overall image size of $100 \times 100 \times 128$. Measured T_2 is ∼650 ns.

intense gradient pulses would enable one to more effectively use spin probes with short T_2, such as nitroxide spin labels, for ESRM applications in various biological and model systems.

4. DISCUSSION

Although ESRM with inductive detection is less sensitive, compared to non-conventional detection methods, such as MRFM or ODESR, sub-micron resolution close to optical resolution, e.g., ∼700 nm is currently obtained with a high concentration spin sample, LiPc, in ambient conditions. This representative sub-micron capability has demonstrated the possibility of sub-micron resolution imaging in biomedical systems with further improvements in methods.

Biological tissue imaging is one of the most promising applications of ESRM. With some modification of our current imaging probe, one can expect to find application of ESRM technology in the analysis of various tissue samples for clinical therapeutic purposes. For cancer research, such as prostate cancer, the tissue architecture can provide valuable information on the determination of cancerous tissue. For example, prostate cancer staging is indicated by information such as the size of the tumor, extent of invaded lymph nodes, and metastasis. Determination of the tissue architecture including the size of the prostate capsule, nerve distribution along the prostatic capsule, etc. is important in clinical applications. ESRM tissue imaging with micron resolution could provide such information. Oxygen imaging of fresh tissue could also be performed by ESRM, which may provide further information on the hypoxia of the cancerous tissue. For cell imaging, ESRM could provide insight on the motility of the cells in various environments, such as chemical gradient, etc. This would be useful to study metastasis of various diseases through blood vessels, and to study the curing mechanisms of damaged tissue and cells.

In summary, sub-micron resolution ESRM has progressed to a state of development where high concentration spin samples can be routinely imaged, and preliminary micron-level resolution ESRM images are now being demonstrated with biomedically relevant samples.

Acknowledgments: We wish to thank A. Singhai, David Holowka, and Barbara Baird of the Cornell University Department of Chemistry and Chemical Biology for providing the sample of RBL cells. We gratefully acknowledge Aharon Blank and Michael Shklyar at the Technion, Haifa, Israel for their earlier contributions to the ESRM Project, and to Sonal Grover, Ashutosh K. Tewari, Leona Cohen-Gould and Frederick R. Maxfield at Weill-Cornell Medical College for their helpful discussions on potential applications of ESRM to prostate cancer. This work was supported by NIH/NCRR Grant P41RR016292 (J. H. Freed) and NIH Grants P41EB002034 and R01 CA98575 (H. J. Halpern).

References and Notes

1. D. Rugar, R. Budakian, H. J. Mamin, and B. W. Chui, *Nature* 430, 329 (**2004**).
2. C. L. Degen, M. Poggio, H. J. Mamin, C. T. Rettner, and D. Rugar, *PNAS* 106, 1313 (**2009**).
3. E. W. Moore, S. G. Lee, S. A. Hickman, S. J. Wright, L. E. Harrell, P. P. Borbat, J. H. Freed, and J. A. Marohn, *PNAS* 106, 22251 (**2009**).
4. C. Shin, C. Kim, R. Kolesov, G. Balasubramanian, F. Jelezko, J. Wrachtrup, and P. R. Hemmer, *J. Lumin.* 130, 1635 (**2010**).
5. G. Balasubramanian, I. Y. Chan, R. Kolesov, M. Al-Hmoud, J. Tisler, C. Shin, C. Kim, A. Wojcik, P. R. Hemmer, A. Krueger, T. Hanke, A. Leitenstorfer, R. Bratschitsch, F. Jelezko, and J. Wrachtrup, *Nature* 455, 648U46 (**2008**).
6. G. Balasubramanian, P. Neumann, D. Twitchen, M. Markham, R. Kolesov, N. Mizuochi, J. Isoya, J. Achard, J. Beck, J. Tissler, V. Jacques, P. R. Hemmer, F. Jelezko, and J. Wrachtrup, *Nat. Mater.* 8, 383 (**2009**).
7. S. Subramanian and M. C. Krishna, *Magn. Reson. Insights* 2, 43 (**2008**).
8. B. Epel, S. V. Sundramoorthy, C. Mailer, and H. J. Halpern, *Magn. Reson. Eng.* 33, 163 (**2008**).
9. B. Epel, C. R. Haney, D. Hleihel, C. Wardrip, E. D. Barth, and H. J. Halpern, *Medical Physics* 37, 2553 (**2010**).
10. A. Blank, C. R. Dunnam, P. P. Borbat, and J. H. Freed, *Appl. Phys. Lett.* 85, 5430 (**2004**).
11. A. Blank and J. H. Freed, *Isr. J. Chem.* 46, 423 (**2006**).
12. A. Blank, C. R. Dunnam, P. P. Borbat, and J. H. Freed, U.S. Patent 7,403,008B2 (**2008**).
13. P. P. Borbat, A. J. Costa-Filho, K. A. Earle, J. K. Moscicki, and J. H. Freed, *Science* 291, 266 (**2001**).
14. J. W. Stoner, D. Szymanski, S. S. Eaton, R. W. Quine, G. A. Rinard, and G. R. Eaton, *J. Magn. Reson.* 170, 127 (**2004**).
15. M. K. Brawer, G. Bartsch, A. V. D'Amico, R. E. Donohue, O. Siam, and A. Tewari, *Rev. Urol*. 5(Suppl. 6), S17 (**2003**).
16. H. J. Halpern, G. V. Chandramouli, E. D. Barth, Y. Cheng, P. Miroslav, J. G. David, and A. T. Beverly, *Cancer Res.* 59, 5836 (**1999**).
17. S. Matsumoto, F. Hyodo, S. Subramanian, N. Devasahayam, J. Munasinghe, E. Hyodo, C. Gadisetti, J. A. Cook, J. B. Mitchell, and M. C. Krishna, *J. Clin. Invest.* 118, 1965 (**2008**).
18. S. K. Yoo, Q. Deng, P. J. Cavnar, Y. I. Wu, K. M. Hahn, and A. Huttenlocher, *Develop. Cell* 18, 226 (**2010**).
19. Y. Matsuda, T. Schlange, E. J. Oakeley, A. Boulay, and N. E. Hynes, *Breast Cancer Research* 11, R32 (**2009**).
20. K. C. Chaw, M. Manimaran, F. E. Tay, and S. Swaminathan, *Microvasc. Res.* 72, 153 (**2006**).
21. A. Blank, C. R. Dunnam, P. P. Borbat, and J. H. Freed, *J. Magn. Reson.* 165, 116 (**2003**).
22. A. Blank, J. H. Freed, N. P. Kumar, and C. H. Wang, *J. Controlled Release* 111, 174 (**2006**).
23. A. Blank, E. Suhovoy, R. Halevy, L. Shtirberg, and W. Harneit, *Phys. Chem. Chem. Phys.* 11, 6689 (**2009**).
24. M. E. Tobar, J. Krupka, E. N. Ivanov, and R. A. Woode, *J. Appl. Phys*. 83, 1604 (**1998**).
25. Y. Deng, S. Petryakov, G. He, E. Kesselring, P. Kuppusamy, and J. L. Zweier, *J. Magn. Reson.* 185, 283 (**2007**).
26. B. Epel, S.V. Sundramoorthy, C. Mailer, and H. J. Halpern, *Magn. Reson. Eng.* 33, 163 (**2008**).
27. B. B. Williams, H. A. Hallaq, G. V. Chandramouli, E. D. Barth, J. N. Rivers, M. Lewis, V. E. Galtsev, G. S. Karczmar, and H. J. Halpern, *Magn. Reson. Med.* 47, 634 (**2002**).
28. Y. Liu, F. A. Villamena, J. Sun, T. Wang, and J. L. Zweier, *Free Radic. Biol. Med.* 46, 876 (**2009**).
29. F. Hyodo, S. Matsumoto, N. Devasahayam, C. Dharmaraj, S. Subramanian, J. B. Mitchell, and M. C. Krishna, *J. Magn. Reson.* 197, 181 (**2009**).

Received: 6 August 2010. Accepted: 2 September 2010.